

MR Neurography of Peripheral Nerve Injury in the Presence of Orthopedic Hardware: Technical Considerations

Darryl B. Sneag, MD • Kelly C. Zochowski, BS • Ek T. Tan, PhD

From the Department of Radiology and Imaging, Hospital for Special Surgery, 535 E 70th St, Room 2P-040, New York, NY 10021. Received October 16, 2020; revision requested December 14; revision received December 29; accepted January 27, 2021. Address correspondence to D.B.S. (e-mail: sneagd@hss.edu).

Conflicts of interest are listed at the end of this article.

Radiology 2021; 300:246–259 • <https://doi.org/10.1148/radiol.2021204039> • Content code: MK

As the frequency of orthopedic procedures performed each year in the United States continues to increase, evaluation of peripheral nerve injury (PNI) in the presence of pre-existing metallic hardware is in higher demand. Advances in metal artifact reduction techniques have substantially improved the capability to reduce the susceptibility effect at MRI, but few reports have documented the use of MR neurography in the evaluation of peripheral nerves in the presence of orthopedic hardware. This report delineates the challenges of MR neurography around metal given the high spatial resolution often required to adequately depict small peripheral nerves. It offers practical tips, including strategies for prescan assessment and protocol optimization, including use of more conventional two-dimensional proton density and T2-weighted fat-suppressed sequences and specialized three-dimensional techniques, such as reversed free-induction steady-state precession and multispectral imaging, which enable vascular suppression and metal artifact reduction, respectively. Finally, this article emphasizes the importance of real-time monitoring by radiologists to optimize the diagnostic yield of MR neurography in the presence of orthopedic hardware.

©RSNA, 2021

Online SA-CME • See www.rsna.org/learning-center-ry

Learning Objectives:

After reading the article and taking the test, the reader will be able to:

- Discuss technical considerations for MR neurography in the presence of metal
- List specialized pulse sequences for both nerve and metal imaging
- Identify and implement troubleshooting methods for MR neurography examinations in which metal artifact may obscure nerve visualization

Accreditation and Designation Statement

The RSNA is accredited by the Accreditation Council for Continuing Medical Education (ACCME) to provide continuing medical education for physicians. The RSNA designates this journal-based SA-CME activity for a maximum of 1.0 AMA PRA Category 1 Credit[®]. Physicians should claim only the credit commensurate with the extent of their participation in the activity.

Disclosure Statement

The ACCME requires that the RSNA, as an accredited provider of CME, obtain signed disclosure statements from the authors, editors, and reviewers for this activity. For this journal-based CME activity, author disclosures are listed at the end of this article.

Peripheral nerve injury (PNI) may result from traumatic or iatrogenic events. Iatrogenic cases in particular contribute to substantial morbidity, long-term disability, and health care costs in the United States (1–3). Traumatic PNI may be associated with anesthetic (1,4,5) and surgical procedures (1), including orthopedic arthroscopy and hardware placement during arthroplasty and fracture fixation (6–13). For example, the prevalence of perioperative nerve injury after hip arthroplasty is 0.17%–7.6%, with increased incidence after revision arthroplasty (14), 0.3%–1.3% for total knee arthroplasty (15), 0%–16% for wrist arthroplasty (6), and 1%–8% for total shoulder arthroplasty (16). Iatrogenic nerve injury has also been reported in the setting of fracture fixation, with rates of radial nerve palsy ranging from 6% to 32% after humeral shaft fixation (17).

As activity has increased in an aging population, demand for orthopedic procedures has also risen (18,19). It is estimated that over 635 000 total hip and 1.26 million total knee arthroplasties will be performed yearly by 2030 (19,20), almost double that of the 370 770 hip and 680 150 knee arthroplasties performed in 2014 (20). As such, a substantial proportion of patients will have pre-existing metallic hardware, whether related to iatrogenic

injury or otherwise, at the time of clinical presentation and imaging for PNI.

Dedicated peripheral nerve MRI, or MR neurography, plays an important role in the clinical management of peripheral neuropathies (21–23). Advances in MRI hardware and software, including the development of multichannel receiver coils and accelerated imaging techniques, have facilitated the overall development of MR neurography as a field and have made imaging around metallic hardware feasible despite distortion from susceptibility effects. While metal artifact reduction techniques in MRI have been widely described (24–27), few reports have documented the use of MR neurography in the presence of metallic hardware (28–30). This report delineates challenges of MR neurography around metal and describes practical techniques to overcome these challenges.

Diagnostic Work-Up of PNI

Clinical management of PNI hinges on determining severity, as more extensive injury is associated with poorer prognosis and may require more immediate surgical intervention (31). PNI is conventionally classified—by increasing severity—as neurapraxia, axonotmesis, or neurotmesis based on the degree of disruption or loss of integrity of

Abbreviations

EMG = electromyography, FSE = fast spin echo, MAVRIC = multiple acquisition variable-resonance image combination, MSDE = motion-sensitized driven equilibrium, MSI = multispectral imaging, PNI = peripheral nerve injury, PSIF = reversed free-induction steady-state precession, SNR = signal-to-noise ratio, STIR = short tau inversion recovery, 3D = three-dimensional

Summary

MR neurography is a useful modality with which to assess peripheral nerve integrity adjacent to orthopedic hardware when imaging protocols are appropriately optimized.

Essentials

- Technical considerations for reducing susceptibility effect from metal include field strength, bandwidth, section thickness, frequency acquisition matrix, and use of dedicated 3D multispectral imaging pulse sequences.
- Technical considerations for MR neurography that are relevant to evaluation of nerves in the presence of metal include performance of high-spatial-resolution, T2-weighted, fat-suppressed, and sometimes vascular-suppressed sequences.
- The combination of technical considerations for metal artifact reduction and high-spatial-resolution peripheral nerve imaging increases the potential diagnostic yield of MR neurography in patients with orthopedic hardware.
- Radiologists must evaluate each case individually to select the appropriate modality, field strength, pulse sequence type, and acquisition parameters.

the nerve microstructure (32). The mildest type of PNI is neuropraxia, in which segmental myelin damage leads to partial or complete conduction block but structural integrity of the nerve is preserved; in this scenario, symptoms typically resolve spontaneously within weeks or months after remyelination (33). Axonotmesis is more severe and involves axonal injury with intact connective tissue and nerve continuity; this type of PNI can be reversed, albeit slowly and sometimes incompletely, via Wallerian degeneration and axonal regeneration at an approximate rate of 1 mm per day (34). However, in severe cases of axonotmesis, surgery may be required. The most severe type of PNI is neurotmesis, typically secondary to nerve transection or severe stretch injury, and necessitates surgical intervention for recovery (34).

Diagnosis: History, Physical Examination, and Electrodiagnostic Studies

Detailed history taking includes time of symptom onset, which is especially relevant given the temporal importance of nerve regeneration and potential intervention (35). For example, primary nerve repair is often preferred within the first 3 weeks after complete nerve transection to minimize complications, such as nerve retraction and fibrosis associated with delayed repair (36–42). Physical examination entails careful assessment for any sensory or motor deficits (35). Electrodiagnostic studies, comprising both nerve conduction studies and electromyography (EMG), are important diagnostic adjuncts commonly used to localize and grade severity of nerve injury. However, the diagnostic utility of EMG is limited by its lack of sensitivity within the first 2 weeks of nerve injury, as Wallerian degeneration and subsequent muscle denervation may take up to 4 weeks to ap-

pear on EMG (43–46). Thus, it may be difficult to differentiate between complete neuropraxic and neurotmetic injury via electrodiagnostic studies alone soon after injury.

Diagnosis: Imaging

High-spatial-resolution US and MR neurography are often used in a complementary fashion to evaluate PNI, but each modality has its own advantages (Table 1) (47–52). The main benefit of dedicated nerve imaging, as compared with electrodiagnostic studies, is its ability to directly localize and depict the extent of nerve injury earlier (53,54). It has been shown that MR neurography can detect muscle denervation by the presence of diffusely increased T2-weighted signal intensity of the muscle as early as 48 hours after insult (in animal models) (55). Furthermore, unlike EMG, in which individual muscles need to be tested and accessible, MRI enables global assessment of regional muscles within one prescribed field of view and can more easily reveal a clinically unsuspected cause of peripheral nerve disease, such as an intrinsic or extrinsic compressive soft-tissue mass (56).

The major advantage of MR neurography over US is its superior contrast resolution. Enhanced nerve-to-background tissue contrast facilitates more reliable identification of peripheral nerves coursing through muscle planes, as well as abnormal changes in the nerve that typically manifest as T2-weighted signal hyperintensity (57,58). US affords higher spatial resolution in the evaluation of superficial nerves and is sometimes the preferred modality when metal resides close to the involved nerve (35); however, segments of deeper nerves, such as the axillary and long thoracic nerves (particularly, as they course through the quadrilateral space and along the chest wall, respectively), and the lumbosacral plexus can typically be visualized only with MRI. US is usually less expensive and less motion dependent but is operator dependent (22). US, however, can sometimes better follow the course of a nerve and better define the soft tissue–metal interface (Fig 1), more reliably depicting the spatial relationship between hardware and adjacent nerves.

Technical Considerations for MR Neurography

MR neurography has evolved through continuous technologic developments over the past decade (50). Most importantly, the availability of 3.0-T magnets and multichannel surface coils enabling high spatial resolution and parallel image acquisition of nerves enabled routine use of MRI to evaluate PNI in the clinical setting (50,59–62). However, due to the need for advanced planning and oversight by radiologists familiar with nerve anatomy and interpretation, widespread clinical use of MR neurography has remained limited.

MR neurography typically comprises two-dimensional high-spatial-resolution proton density or T1-weighted images to accentuate anatomic details, including fascicular architecture of nerves, as well as T2-weighted fat-suppressed sequences (Tables 2, 3). As proton density sequences inherently provide higher SNR than T1-weighted sequences, proton density sequences can achieve higher spatial resolution for a given acquisition time. Additionally, as the proton density sequences applied in our protocols have some inherent T2 weighting (echo time, 35 msec), they provide additional contrast resolution to depict abnormal

changes in nerves when compared with T1-weighted sequences. T2 weighting accentuates nerve abnormality, and fat suppression provides an appropriate intensity range for high conspicuity of nerves relative to background soft tissues. Images orthogonal to the longitudinal axis of the nerve are routinely acquired to confidently assess fascicular architecture and morphology given the sometimes circuitous course of peripheral nerves.

For fat suppression in two-dimensional imaging, a Dixon method-based (63) fat-water separation fast spin-echo (FSE) technique is often preferred due to its high signal-to-noise ratio (SNR) and robustness to B_1 inhomogeneous anatomies, such as the curvature at the neck and shoulder junction and at the ankle that create challenges for chemical fat-saturation techniques (63,64). Dixon fat-suppression sequences, typically performed with two echoes, usually require coupling with parallel imaging to decrease long acquisition times (48,65). Short tau inversion recovery (STIR) sequences also provide robust fat suppression relative to chemical fat saturation but suffer from lower SNR (64).

Vascular suppression is important for visualization of certain branch nerves off the brachial and lumbosacral plexi, as well as smaller peripheral nerves that run alongside blood vessels that can be confounders due to their similar size and signal intensity. In the periphery, a useful sequence is a fluid-sensitive FSE three-dimensional (3D) gradient-echo-based technique known as reversed free-induction steady-state precession (PSIF) (66,67) that uses frequency selective fat suppression

on Siemens Healthineers platforms but that has been combined with a Dixon fat-suppression scheme as a prototype on GE Healthcare platforms. Regardless of the fat-suppression scheme, PSIF is motion sensitive and therefore tends not to work well around the chest wall and pelvic regions. Thus, it may be advantageous to use FSE readouts in these regions, as FSE not only boasts higher SNR but is also less prone to motion artifacts due to refocusing of dephased spins with the application of refocusing pulses. When 3D images are acquired with a variable flip angle (68), the technique is known by various vendor acronyms, including CUBE (General Electric), SPACE (Siemens), or VISTA (Philips). The 3D FSE sequences can yield images with isotropic high in-plane resolution for reconstruction in arbitrary planes to depict frequently tortuous nerve trajectories. In combination with 3D FSE, a standard chemical fat-saturation preparation pulse could be used to suppress fat, but it often suffers from incomplete fat suppression due to highly varying B_0

Table 1: Comparison of Clinical Considerations for MR Neurography and US for Evaluating Peripheral Nerve Injury

Consideration	MR Neurography	US
Real-time or dynamic study	Inferior	Superior
Easy to compare with contralateral side	Inferior	Superior
Contrast resolution	Superior	Inferior
Spatial resolution (for superficial nerves)	Inferior	Superior
Visualization of deeper nerves (axillary, long thoracic)	Superior	Inferior
Simultaneous visualization of multiple nerves	Superior	Inferior
Motion artifact susceptibility	Inferior	Superior
Metal (susceptibility) distortion	Slightly inferior	Superior
Muscle evaluation	Superior	Inferior
Quantitative analysis	Superior	Inferior
Operator dependency	Slightly superior	Slightly inferior
Cost	Inferior	Superior
Patient access	Slightly inferior	Slightly superior

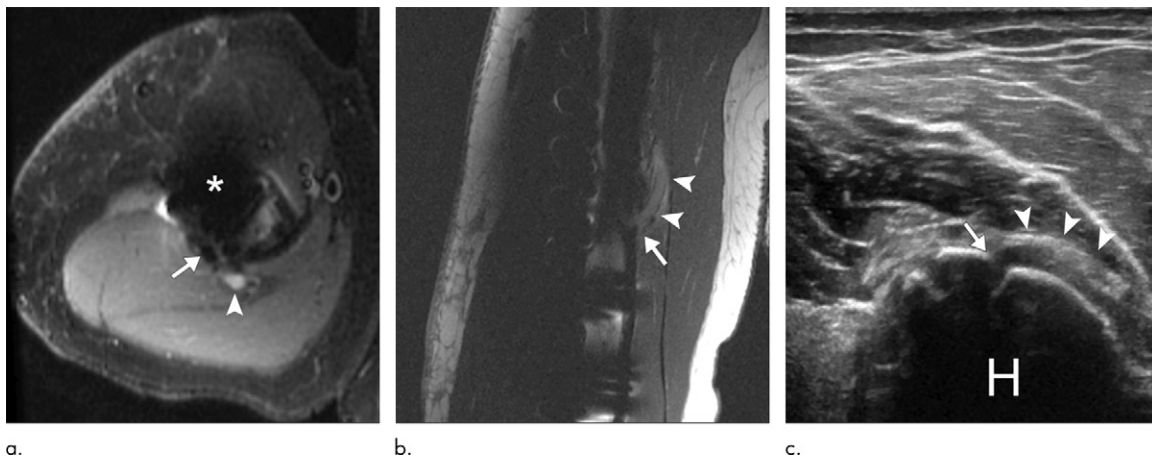


Figure 1: Images in a 41-year-old man with radial nerve palsy after internal fixation of a humerus shaft fracture. **(a)** Axial short inversion time inversion-recovery and **(b)** coronal proton density 1.5-T images show signal hyperintensity of the radial nerve (arrowheads) as it courses through the spiral groove at the level of the humeral plate (*). On **b**, the nerve appears entrapped at the fracture site (arrow). **(c)** Gray-scale US image enables confirmation of entrapment (arrow) of the radial nerve (arrowheads) within a cortical fracture window in the humerus (H). (Precise parameters were not available for these images).

Table 2: Unilateral Brachial Plexus/Bilateral Lumbosacral Plexus Example MR Neurography Protocols for Imaging Near Metal at 3.0 T

Sequence Parameter	2D Proton Density FSE		2D T2-weighted FSE		3D T2-weighted FSE		3D Proton Density MAVRIC-SL	3D IR MSI MAVRIC-SL
	Metal Absent	Metal Present	Metal Absent	Metal Present	Metal Absent	Metal Present	Metal Present	Metal Present
Repetition time/echo time (msec)	3500–6000/35	3500–6000/35	3500–6000/85	3500–6000/85	3000–4000/60–80	3000–4000/60–80	3500–6000/8	3500–6000/60
Field of view (cm)	28–30	28–30	16–28	16–28	25.6–29	25.6–29	25–30	25–30
Matrix size*	512 × 352	512 × 352	320 × 192–224	320 × 192–224	256 × 256–292	256 × 256–292	320 × 256	320 × 256
No. of sections	54–70	54–70	30–40	30–40	90–120	90–120	36	36
Section thickness (mm) (no gap)	3.5–4.5	2.5–3.5	2.5–3.0	2.5–3.0	1.0–1.4	1.0–1.4	3.5	3.5
Echo train length	10–15	10–15	12–16	12–16	130	130	48	20
Bandwidth (Hz/pixel)	195	313–488	391 absent,	391–500	343–391	343–391	781	781
Fat-suppression technique	None	None	Dixon absent,	Dixon or STIR (inversion time = 250 msec)	STIR (inversion time = 250 msec)	STIR (inversion time = 250 msec)	None	STIR (inversion time = 250 msec)
No. of excitations or phase oversampling	2	2	2	2	1	1	0.5 (partial Fourier factor)	0.5 (partial Fourier factor)
Parallel imaging factor	1.75	1.75	1–1.5		None		1.5–2.0	1.5–2.0
Imaging plane	Axial	Axial	Brachial-plexus: coronal, oblique sagittal; lumbosacral plexus: axial, oblique coronal, oblique sagittal	Brachial-plexus: coronal, oblique sagittal; lumbosacral plexus: axial, oblique coronal, oblique sagittal	Oblique coronal	Oblique coronal	Axial, oblique coronal, oblique sagittal	Axial, oblique coronal, oblique sagittal
Other parameters	None	None	Brachial-plexus: respiratory triggering (optional) [†]	Brachial-plexus: respiratory triggering (optional) [†]	Saturation bands	Saturation bands	No. of bins up to 24, 12-kHz offset	No. of bins up to 24, 12-kHz offset
Acquisition time (min)	3–5	3–6	4–7 depending on use of respiratory triggering	4–7 depending on use of respiratory triggering	7–10	7–10	6–8	6–8

Note.—For both the brachial plexus and lumbosacral plexus, 32-element receive-only coils are preferable. FSE = fast spin echo, IR = inversion recovery, MAVRIC-SL = Multiple-acquisition variable-resonance image combination (GE Healthcare platforms), SE = section encoding, STIR = short tau inversion recovery, 3D = three-dimensional, 2D = two-dimensional.

* Matrix size = frequency encoding × phase encoding.

[†] Source.—Reference 96.

Table 3: Extremity Example MR Neurography Protocol for Imaging Near Metal at 3.0 T

Sequence Parameter	2D Proton Density FSE		2D T2-weighted FSE		3D T2-weighted Gradient Echo (PSIF)	3D Proton Density MAVRIC-SL	3D IR MAVRIC-SL
	Metal Absent	Metal Present	Metal Absent	Metal Present	Metal Absent	Metal Present	Metal Present
Repetition time/echo time (msec)	3500–6000/35	3500–6000/35	3500–6000/80	3500–6000/80	9.5/5	3500–6000/8	3500–6000/60
Field of view (cm) (variable depending on size of extremity)	6–16	6–16	8–16	8–16	10–12	18	18
Matrix size*	512 × 352	512 × 352	320 × 224	320 × 224	320–224	320 × 256	320 × 256
No. of slices	54–70	54–70	30–40	30–40	90	36	36
Section thickness (mm) (no section gap)	2.5–3.5	2.0–3.0	2.5–3.0	2.5–3.0	2.0	3.5	3.5
Echo train length	10–15	10–15	12–16	12–16	1	48	20
Bandwidth (Hz per pixel)	195	313–488	391	391–500	122	781	781
Fat-suppression technique	None	None	Dixon	Dixon or STIR (TI = 250 ms)	Dixon	None	STIR (TI = 250 ms)
No. of excitations or phase oversampling	2	2	2	2	1	0.5 (partial Fourier factor)	0.5 (partial Fourier factor)
Parallel imaging factor	1.75	1.75	1–1.5	1–1.5	2	1.5–2.0	1.5–2.0
Imaging plane	Axial	Axial	Axial	Sagittal or coronal	Axial	Axial	Axial
Other parameters	None	None	None	None	None	No. of bins up to 24, 12-kHz offset	No. of bins up to 24, 12-kHz offset
Acquisition time (min)	3–5	3–6	4–6	4–6	6	8	8

Note.—Sixteen-channel receive-only coils are preferable. FSE = fast spin echo, IR = inversion recovery, MAVRIC-SL = multiple-acquisition variable-resonance image combination (GE Healthcare platforms), PSIF = reversed free-induction steady-state precession (prototype sequence on GE Healthcare platforms, courtesy of Daehyun Yoon from Stanford University), SE = section encoding, 3D = three-dimensional, 2D = two-dimensional.

* Matrix size = frequency encoding × phase encoding.

inhomogeneities in the chest and pelvic regions. Therefore, in these regions, a 3D gadolinium-enhanced, STIR fat-suppressed long-echo-time FSE sequence (69) could be used to achieve robust fat suppression by nulling longitudinal magnetization of fat while suppressing signal arising from blood vessels containing gadolinium (70,71). While the STIR fat-suppressed long-echo-time FSE sequence could also be effectively used without contrast agents, vascular suppression would need to be affected to avoid confounding vascular signal that bears resemblance to that of nerves. One way is to add additional crusher gradients alongside the refocusing pulses, effectively providing diffusion weighting that suppresses flow in vessels. Another method is to use a motion-sensitized driven equilibrium (MSDE) technique, which applies an additional preparation pulse prior to the FSE readout (72). The downside of noncontrast vascular suppression

is increased sensitivity to B_1 inhomogeneities (MSDE), reduced SNR (crushers and MSDE), reduced sensitivity to bulk motion artifacts (crushers and MSDE), and increased blurring from increased FSE echo spacing (crushers), all of which make higher-spatial-resolution imaging more challenging. In our practice, vascular-suppressed 3D sequences are used as adjuncts to standard two-dimensional FSE sequences when visualization of smaller caliber nerves is needed.

Intravenous gadolinium-containing contrast agents for purposes other than vascular suppression and angiography are frequently not needed for MR neurography. Circumstances in which T1-weighted contrast-enhanced sequences can be helpful, however, are evaluation of the presence and extent of a postoperative fluid collection (eg, seroma or abscess) or scar tissue, which may entrap nerves, compress them, or both. Postcontrast T1-weighted

Table 4: Summary of General Technical Considerations for MRI Around Metal

Technical Parameter	Description of Considerations
Field strength	1.5 T generally preferable to 3.0 T as susceptibility is directly proportional to magnetic field strength (B_0) (97). 3.0 T, however, provides higher SNR than 1.5 T. 3.0 T generally preferred in MR neurography due to higher spatial resolution requirements, particularly when the nerve or nerves in question are sufficiently distant from hardware (Fig 2)
Position of hardware in magnet	Image distortion can be reduced by directly aligning hardware with B_0 and placement of anatomy at isocenter. Ability to freely position is limited due to hardware location and constraints from finite magnet bore diameter (24)
Readout bandwidth	Increasing bandwidth reduces distortion. Increased bandwidth reduces signal-to-noise ratio, which can be mitigated by increasing the number of acquisitions (24)
Voxel size	Decreasing section thickness or increasing the frequency acquisition matrix will decrease voxel size, which reduces local B_0 variation within each voxel and intravoxel signal decay (24)
Use of specialized pulse sequences, such as multispectral imaging	Three-dimensional multispectral imaging techniques, such as multiple-acquisition variable-resonance image combination (MAVRIC), section encoding for metal artifact correction (SEMAC), and their hybrid sequence (MAVRIC-SL) can be applied to generate images with high signal-to-noise ratio with high spatial and contrast resolution and section location selectivity (99)

Note.—SNR = signal-to-noise ratio.

imaging also helps provide an appropriate intensity contrast range for delineating soft-tissue anatomy (eg, nerves and muscles) in the presence of adjacent metallic hardware. For instance, T1-weighted postcontrast images can sometimes be helpful to determine the presence of a neuroma, a disorganized and unsuccessful attempt by a nerve to regenerate, which may sometimes enhance (73).

MR Neurography in the Presence of Metallic Hardware: Suggested Parameter Modifications and Techniques

It is challenging to perform MRI near orthopedic hardware due to strong magnetic susceptibility artifacts (74–78), which manifest as in-plane and through-plane image distortions, voxel pile-up image artifacts, ripples, and signal voids (74). The extent of and technical considerations for mitigating these artifacts increase with (a) increased magnetic susceptibility of the hardware and (b) increased proximity of the imaged tissue to the metal (79–81). Image quality, however, has improved over the past 2 decades due to several technical advancements, which are summarized in Table 4 (24,80,82–84).

Literature on the use of MR neurography in the presence of metal is sparse, but early reports have described sensitivities of 86%–93% and positive predictive values of 87%–97% for imaging of the lumbosacral plexus and sciatic nerve (28,30). Suggested parameter modifications for MR neurography in the presence of metal are summarized in Tables 2 and 3. By integrating technical considerations for MR neurography with those for MRI around metal, MRI examination of a patient with indwelling hardware suspected of having PNI can be optimized via two separate but interrelated aspects: (a) a prescan assessment and (b) imaging protocol modifications.

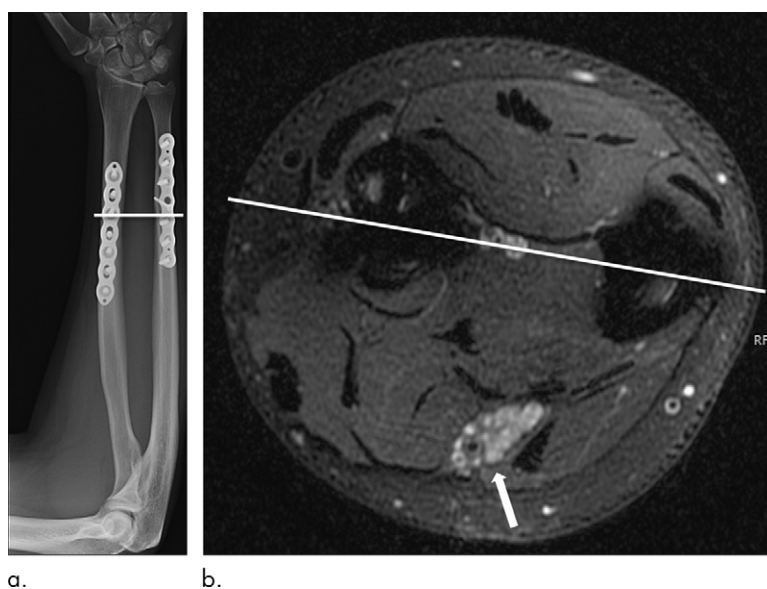


Figure 2: Images in a 19-year-old man with fixation plates in the radius and ulna (transected by white line) 1 year after a motor vehicle collision who presented with persistent ulnar neuropathy after nerve grafting. **(a)** Review of radiographs during a prescan assessment and clinical notes suggested that the nerve in question was sufficiently distant from the metal (white line) and would likely not require 1.5-T or specialized metal artifact reduction sequences. **(b)** Axial 3.0-T Dixon (repetition time msec/echo time msec, 5734/81; bandwidth, 244 Hz per pixel; spatial resolution, $0.31 \times 0.45 \times 2$ mm; acquisition time, 4.0 minutes) water image enables clear visualization of an enlarged hyperintense ulnar nerve (arrow).

Prescan Assessment

Clinical notes, electrodiagnostic reports, and results of prior imaging should be reviewed to determine the nerve or nerves in question, the expected location of the nerve injury, and the expected position of the nerve (based on its known anatomic course) relative to the hardware. This information then guides customized planning of the type or types of examination to be performed, including if MRI is the most appropriate modality, and if so, the appropriate field strength and scan coverage to maximize diagnostic yield.

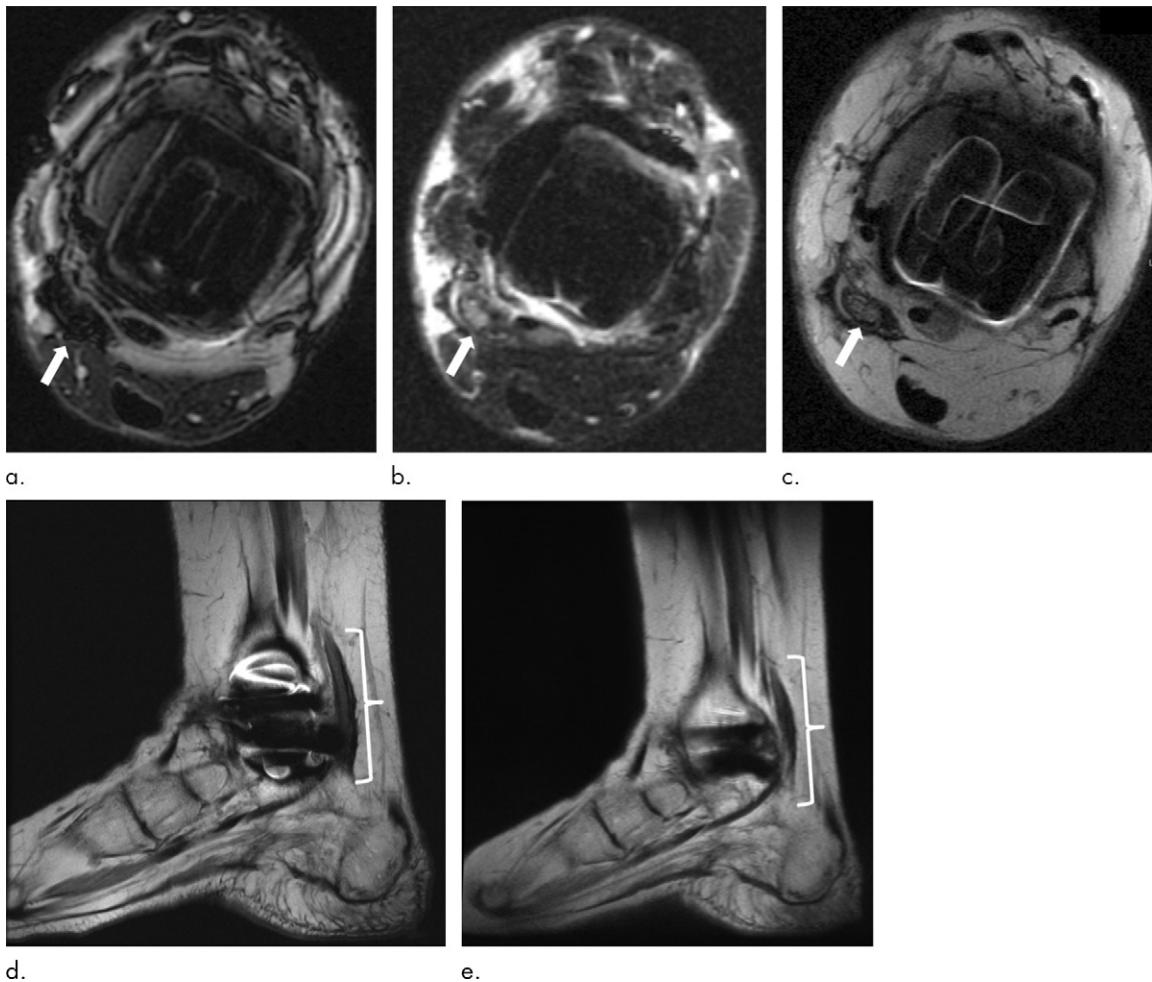


Figure 3: Images in a 52-year-old woman presenting with paresthesia in the toes after left total ankle arthroplasty 5 years earlier. A 1.5-T field strength was chosen to start, as the susceptibility effect of the arthroplasty was predicted to obscure the tibial nerve at 3.0 T. **(a)** Axial 1.5-T Dixon water image (repetition time msec/echo time msec, 5895/90; bandwidth, 325 Hz per pixel; resolution, $0.59 \times 0.78 \times 2.5$ mm; acquisition time, 6.5 minutes) shows susceptibility effect obscuring the tibial nerve (arrow). Axial **(b)** short tau inversion-recovery (5422/14; bandwidth, 651.016 Hz per pixel; resolution, $0.59 \times 0.78 \times 3.0$ mm; acquisition time, 6.8 minutes) and **(c)** proton density (6014/25; bandwidth, 488 Hz/pixel; resolution, $0.29 \times 0.47 \times 3.3$ mm; acquisition time, 7.4 minutes) images show the tibial nerve was best visualized where the nerve demonstrated fascicular enlargement and hyperintensity of indeterminate origin. Note the sharper image quality due to lower interecho spacing and higher in-plane resolution on **(d)** conventional sagittal proton density image (4025/24; bandwidth, 488 Hz per pixel; resolution, $0.33 \times 0.56 \times 3.0$ mm; acquisition time, 6.5 minutes) compared with **(e)** the multiple-acquisition variable-resonance image combination (MAVRIC-SL) proton density image (4000/8.1; bandwidth, 488 Hz per pixel; resolution, $0.43 \times 0.98 \times 3.0$ mm; acquisition time, 4.7 minutes) that makes the dense epineurial scar (brackets) of the tibial nerve more conspicuous. Decreased susceptibility artifact on **e**, however, better shows the perineural fat and spatial resolution of the arthroplasty relative to the tibial nerve.

Modality.—After reviewing all available documents, the radiologist setting the protocol may decide that US or CT is more appropriate than MRI, at least initially. US may be recommended after review of the radiographs and patient history if magnetic susceptibility effects are expected to overwhelm visualization of the nerve despite modifications to the MRI protocol. Additionally, if extensive heterotopic ossification is seen on radiographs, CT may be recommended to determine the extent of this ossification and its relationship to adjacent nerves. In cases with no apparent contraindications and when superior contrast resolution is desired, MRI is the preferred modality for PNI assessment and can be optimized through careful planning by the radiologist.

Field strength.—Imaging orthopedic hardware at both 1.5 and 3.0 T is subject to MRI safety recommendations accord-

ing to the manufacturer's guidelines. Most orthopedic hardware is safe from projectile risk due to the fixed nature of these implants (85). MRI conditional hardware is also subject to radiofrequency heating or spontaneous absorption rate and gradient slew rate limitations; however, implant heating is a nonissue for clinical imaging at both 1.5 and 3.0 T (86). At 3.0 T, MRI affords almost double the SNR as 1.5-T MRI, which helps facilitate optimal spatial resolution (Fig 2). At our institution, 1.5-T MRI is the first choice when the primary clinical goal is to evaluate osseous integration of arthroplasties and surrounding soft tissue, as 1.5-T MRI minimizes the susceptibility effect of the implant (Fig 3). However, when the primary concern is PNI, the field strength is chosen based on the nerve in question, the adjacent hardware, and the spatial relationship between the two. For brachial

plexus evaluation in the presence of a shoulder arthroplasty (Fig 4) and for evaluation of the femoral (Fig 5) and sciatic (Fig 6) nerves in the presence of a hip arthroplasty, 3.0-T MR neurography is favored over 1.5-T MR neurography,

as nerves can be better visualized at 3.0 T despite increased artifacts from adjacent hardware. For PNI adjacent to knee and ankle arthroplasties, 1.5-T MR neurography is preferable, as susceptibility effect in the axial plane (orthogonal to

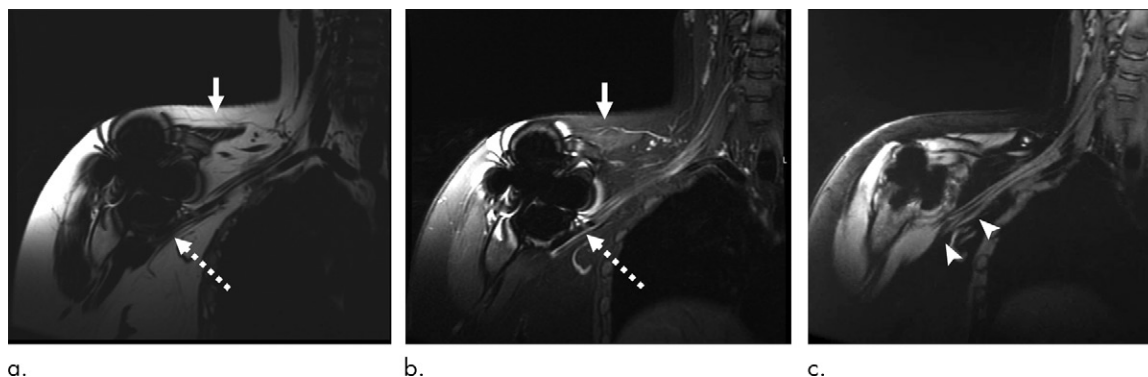


Figure 4: Images in a 21-year-old woman with pain radiating down her right arm after resurfacing shoulder arthroplasty 15 months prior. Coronal **(a)** water and **(b)** fat 3.0-T reconstructed Dixon (repetition time msec/echo time msec, 4823/88; bandwidth, 488 Hz per pixel; resolution, $0.91 \times 1.5 \times 3.0$ mm; acquisition time, 6.8 minutes) images show most of the brachial plexus, with the exception of terminal branches due to distortion from the arthroplasty (dashed arrow) but demonstrate a complete fat-water swap (solid arrow) due to the presence of metal (compare **a** and **b**). **(c)** Multiple-acquisition variable-resolution combination inversion recovery (5138/8.5; bandwidth, 488 Hz per pixel; resolution, $0.94 \times 1.6 \times 3.5$ mm; 6.8 minutes) dramatically reduces the susceptibility effect and facilitates visualization of the terminal branches (arrowhead).

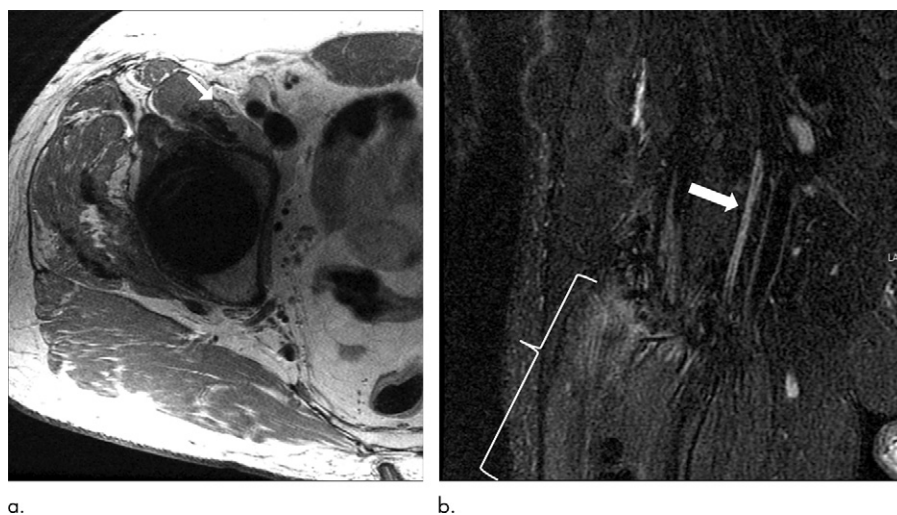


Figure 5: Images in a 52-year-old man with right quadriceps weakness after right total hip arthroplasty via anterior approach 5 months earlier. **(a)** Axial proton density (repetition time msec/echo time msec, 4458/29; bandwidth, 391 Hz per pixel; resolution, $0.43 \times 0.69 \times 2$ mm; acquisition time, 5.5 minutes) and **(b)** coronal Dixon (4124/89; bandwidth, 326 Hz per pixel; resolution, $0.68 \times 0.98 \times 1.5$ mm; acquisition time, 3.2 minutes) 3.0-T images show the femoral nerve proper (arrow) is well depicted and hyperintense as it leaves the pelvis. Distal muscular branches (not shown) of the femoral nerve were entrapped by scar tissue (bracket).

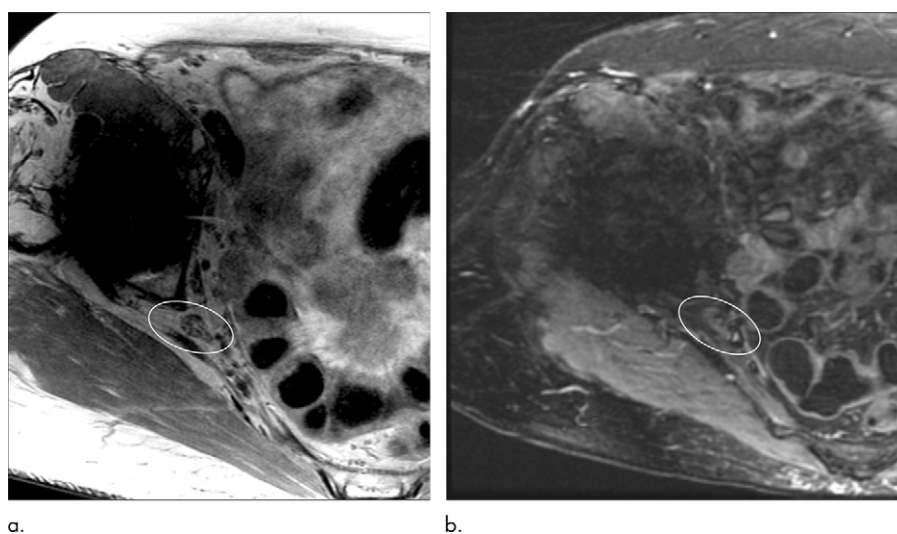


Figure 6: Images in a 79-year-old woman who presented with difficulty walking thought to be due to iliopsoas bursitis after right total hip arthroplasty via a posterior approach 9 years prior. Axial **(a)** proton density (repetition time msec/echo time msec, 5683/31; bandwidth, 326 Hz per pixel; resolution, $0.45 \times 0.72 \times 4.5$ mm; acquisition time, 4.7 minutes) and **(b)** inversion recovery (4526/19; bandwidth, 488 Hz per pixel; resolution, $0.90 \times 1.2 \times 4.5$ mm; acquisition time, 5.7 minutes) 3.0-T images show the sciatic nerve (oval) within the greater sciatic foramen, and it appears normal. For MR neurography, and for musculoskeletal imaging in general, fluid-sensitive sequences (eg, inversion recovery sequences) are used to increase sensitivity to pathologic changes but are combined with higher spatial resolution proton density images to delineate morphology.

most nerves in these regions) can be overwhelming at 3.0 T (Fig 3). However, a protocol for each examination is established on a case-by-case basis, and exceptions to these general guidelines can be made. Occasionally, if susceptibility effect unexpectedly obscures visualization of a nerve during a case that was started at 3.0 T, the patient can be reimaged at 1.5 T as time and scanner availability allow (Fig 7). As such, all MR neurography examinations, particularly those around metallic hardware, may require careful real-time monitoring by a radiologist specializing in MR neurography.

Scan coverage.—When iatrogenic injury is suspected, it is critical to scan the appropriate anatomic region to evaluate the nerve in question and the surgical site. For example, brachial plexus MRI may be ordered to evaluate the axillary nerve after glenohumeral capsular repair, as the standard coverage for brachial plexus MRI may cover only the extraforaminal roots to the beginning of the terminal branches. However, upon careful review of the surgical history and inspection of the surgical

site, coils can be placed in the appropriate position over the shoulder region to properly depict the axillary nerve as it enters the quadrilateral space, and the field of view prescribed can be minimized to maintain high spatial resolution. Skin markers are typically placed at the proximal and distal ends of a surgical incision as a guide to the technologist and supervising radiologist to focus on the imaged region.

Optimization of Imaging Protocols

Radiologists must also be proactive in optimizing imaging protocols before and during the examination. In some practices, it may not be feasible for radiologists to routinely monitor studies in real time, and as such, technologists should also be educated on relevant anatomy and protocol optimization to ensure that the clinical question is appropriately addressed. We have outlined some common scenarios in this article; however, exceptions are likely to occur in the clinical setting, and radiologists must be prepared to adopt a creative approach.

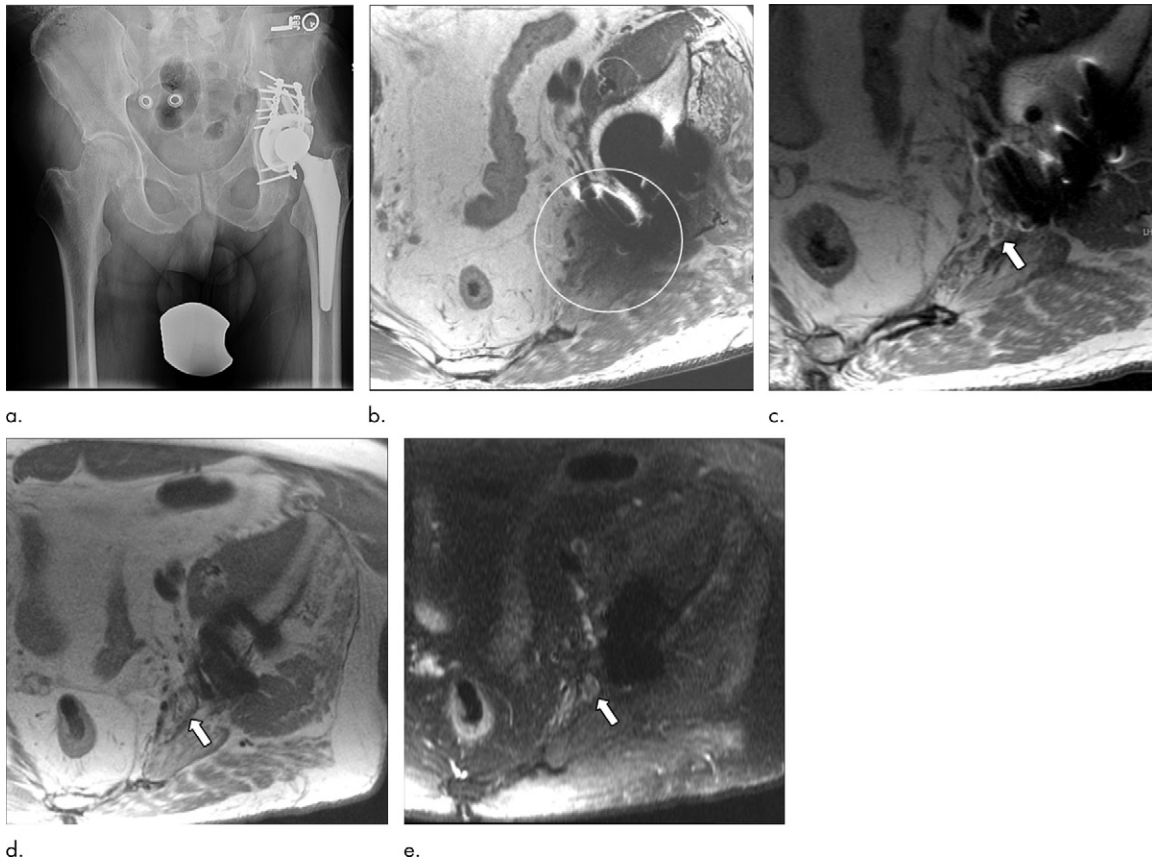


Figure 7: Images in a 73-year-old man with left lower extremity pain, left foot burning sensation, and gluteal weakness after left acetabular fixation and posterior approach total hip arthroplasty. **(a)** Pelvic radiograph shows left total hip arthroplasty in the expected position, along with the fixation hardware. **(b)** MR neurography at 3.0 T (repetition time msec/echo time msec, 4487/34; bandwidth, 488 Hz per pixel; resolution, $0.43 \times 0.63 \times 3.0$ mm; acquisition time, 7.9 minutes) is generally chosen as the optimal field strength to evaluate the sciatic nerve after arthroplasty, but the nerve was obscured by artifact at the level of the greater sciatic foramen (s) due to an additional artifact from acetabular fixation hardware. **(c)** The patient was subsequently imaged at 1.5 T (4432/26; bandwidth, 488 Hz per pixel; resolution, $0.43 \times 0.86 \times 3.0$ mm; acquisition time, 7.8 minutes), and the nerve (arrow) was only partially visualized using a conventional oblique proton density sequence. Oblique sagittal **(d)** multiple acquisition variable-resonance image combination (MAVRIC) proton density (3500/10; bandwidth, 488 Hz per pixel; resolution, $0.78 \times 0.78 \times 3.0$ mm; acquisition time, 4.9 minutes) and **(e)** MAVRIC short inversion time inversion-recovery (4234/7.6; bandwidth, 488 Hz per pixel; resolution, $0.75 \times 1.9 \times 3.0$ mm; acquisition time, 9.2 minutes) sequences at 1.5 T cleared up all distortion and depicted a hyperintense and mildly swollen sciatic nerve (arrow) not impinged on by metal within the foramen, presumably related to retraction injury at the time of acetabular fixation hardware placement.

Use of metal artifact reduction techniques in MR neurography.—The first step in metal artifact mitigation is to increase the readout bandwidth. Non-negligible magnetic susceptibility from metal results in localized frequency off resonance that in turn results in susceptibility effects, such as image distortion and signal void. Therefore, doubling the receiver bandwidth would proportionately diminish susceptibility effects by half (Fig 8). However, doubling the bandwidth without changing the field of view or spatial resolution would decrease SNR by 30%, as SNR is inversely proportional to the square root of bandwidth. Therefore, if metallic artifacts are severe, it would be impractical to use too large a bandwidth, as SNR would be severely diminished.

Another option is to use specialized 3D multispectral imaging (MSI) sequences (eg, multiple acquisition variable-resonance image combination [MAVRIC] or slice encoding for metal artifact correction, or SEMAC (Fig 9). Although these sequences were primarily developed to assess osseous

integration of implants and surrounding soft tissues, they can also be used in MR neurography to reduce artifacts caused by orthopedic hardware in cases where an artifact obscures direct visualization of the nerves being interrogated (Fig 3). However, if the nerves in question are not expected to be affected by image distortion, these sequences may not be necessary, and standard MR neurography sequences can be applied (Fig 10). The decision to employ specialized sequences relies on the radiologist's experience in anticipating the severity of the artifact produced by a particular hardware type and its proximity to the nerve or nerves. The disadvantage of 3D MSI sequences, as compared with traditional two-dimensional ones, is that 3D sequences typically suffer from lower in-plane resolution. Additionally, 3D MSI necessitates longer scan times due to the need for multiple acquisitions corresponding to the number of frequency bins that must be acquired. To mitigate lengthy scanning times, longer echo train lengths are used; however, this results in longer interecho spacing and blurring (Fig 3). Spatial resolution may also be reduced relative to non-MSI 3D

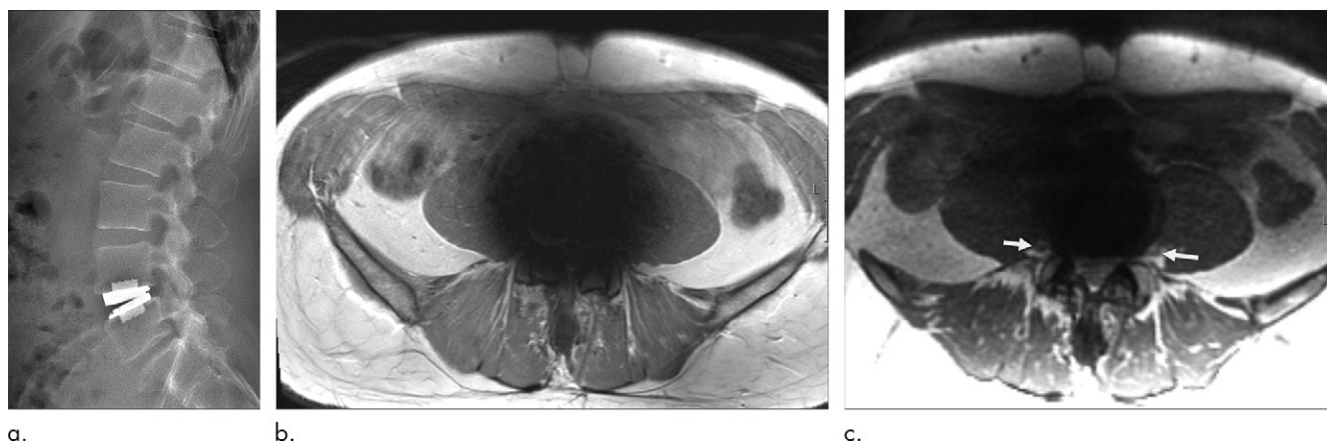


Figure 8: Images in a 46-year-old man with low back pain radiating down both legs after L4–5 intervertebral disc replacement. **(a)** Lateral lumbar spine radiograph. **(b, c)** Axial proton density (repetition time msec/echo time msec, 5290/29 msec; resolution, $0.57 \times 0.91 \times 4.5$ mm; acquisition time, 7.2 minutes) images of the lumbar plexus at 3.0 T obtained with different bandwidths (325.5 Hz per pixel in **b**, 976.6 Hz per pixel in **c**) show visualization of the extraforaminal L4 nerve roots (arrows) only on **c**.

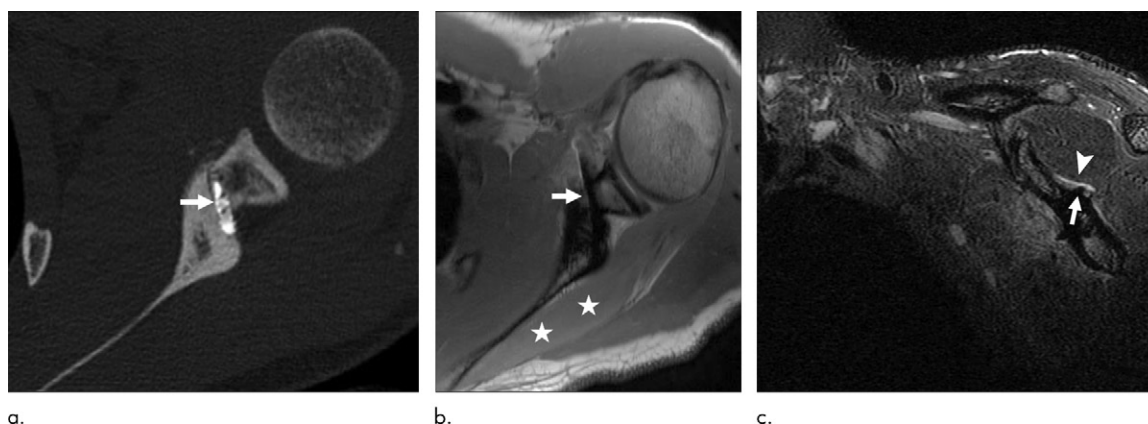


Figure 9: Images in a 19-year-old man with suprascapular neuropathy after Bristow-Latarjet coracoid transfer procedure performed 3 months earlier show a fixation screw (arrow) projecting into the spinoglenoid notch on **(a)** axial CT and **(b)** 3.0-T proton density MRI scans. Note selective denervation edema pattern of the infraspinatus muscle (*****). **(c)** Coronal multiple acquisition variable-resonance image combination inversion recovery image shows direct focal impingement by the screw (arrow) on the suprascapular nerve (arrowhead). (Precise parameters were not available for these images.)

sequences, and a fast calibration scan can be prescribed to reduce the number of frequency bins required (87).

Use of Dixon versus inversion recovery sequences.—Some cases may permit evaluation of peripheral nerves with two-point Dixon sequences at either 3.0 or 1.5 T when metal is present. For example, if a radiologist determines that MAVRIC is not needed due to the spatial relationship between the nerve of interest and the metallic artifact, the Dixon sequence may be allowable without a substantial susceptibility effect impacting nerve visualization (Fig 2). Susceptibility effects may cause the image phase to be wrapped or aliased, but phase unwrapping algo-

rithms are often robust in unaliasing the phase (88). The Dixon FSE sequence works by acquiring two or more sets of FSE readouts, whereby one or more readouts are shifted by the appropriate interval to provide out-of-phase images (89). One important phenomenon to be cognizant of when using Dixon sequences is complete fat-water swaps (Fig 4). These can occur when the magnetic field becomes inhomogeneous due to the presence of metal, causing the fat to appear as if it were replaced by the water signal and vice versa due to the dominance of the off-resonant signal, which confuses the Dixon algorithm. Nevertheless, this problem can be easily mitigated by interpreting the fat image rather than the water image.

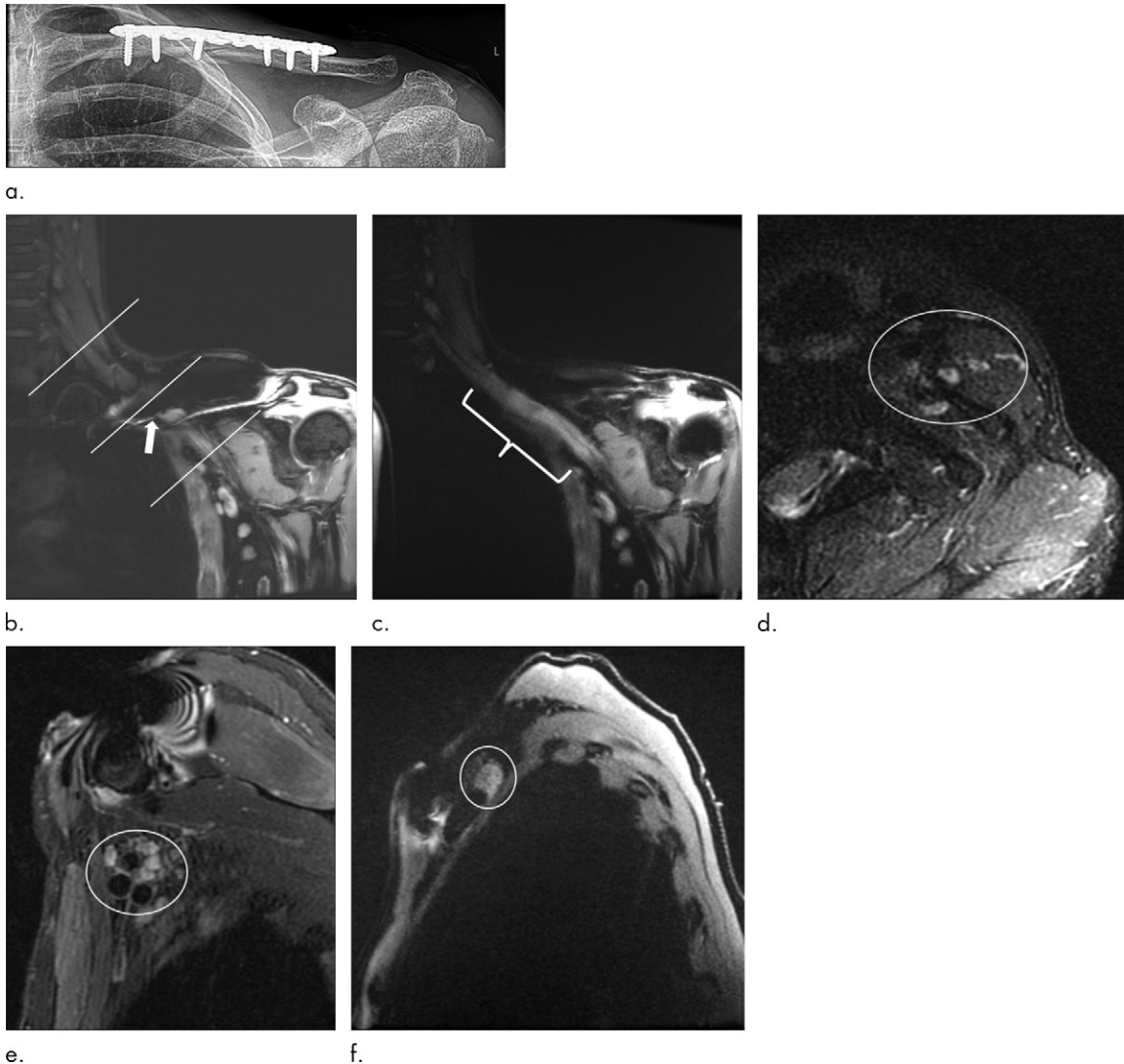


Figure 10: Images in a 52-year-old woman who is unable to move her left hand and fingers after clavicular plate fracture fixation. **(a)** Frontal radiograph shows left clavicular plate and screw fixation in the expected position. **(b)** Conventional coronal 3.0-T inversion recovery (repetition time msec/echo time msec, 4106/11; bandwidth, 1.63 Hz per pixel; resolution, $0.69 \times 0.86 \times 3.5$ mm; acquisition time, 3.9 minutes) image shows the brachial plexus (arrow) was not well visualized. Oblique sagittal sequences, as part of a routine plexus protocol, are prescribed orthogonal to the long axis of the plexus (white lines) **(c)** The multiple acquisition variable-resonance image combination (MAVRIC) inversion recovery (5130/9.1; bandwidth, 488 Hz per pixel; resolution, $0.69 \times 0.86 \times 3.5$ mm; acquisition time, 7.7 minutes) enabled the radiologist to identify diffuse thickening and signal hyperintensity of the plexus, thought to reflect stretch injury (bracket). T2 Dixon sequences were obtained **(d)** proximal (6006/81; bandwidth, 244 Hz per pixel; resolution, $0.5 \times 0.71 \times 2.5$ mm; acquisition time, 4.6 minutes) and **(e)** distal (10 000/89; bandwidth, 244 Hz per pixel; resolution, $0.5 \times 0.71 \times 2.5$ mm; acquisition time, 5.0 minutes) to the metal, and **(f)** MAVRIC IR technique (4376/9.7; bandwidth, 488 Hz per pixel; resolution, $0.56 \times 0.70 \times 3.0$ mm; acquisition time, 8.2 minutes) was used at the level of the plate to minimize susceptibility effect and image the plexus (o).

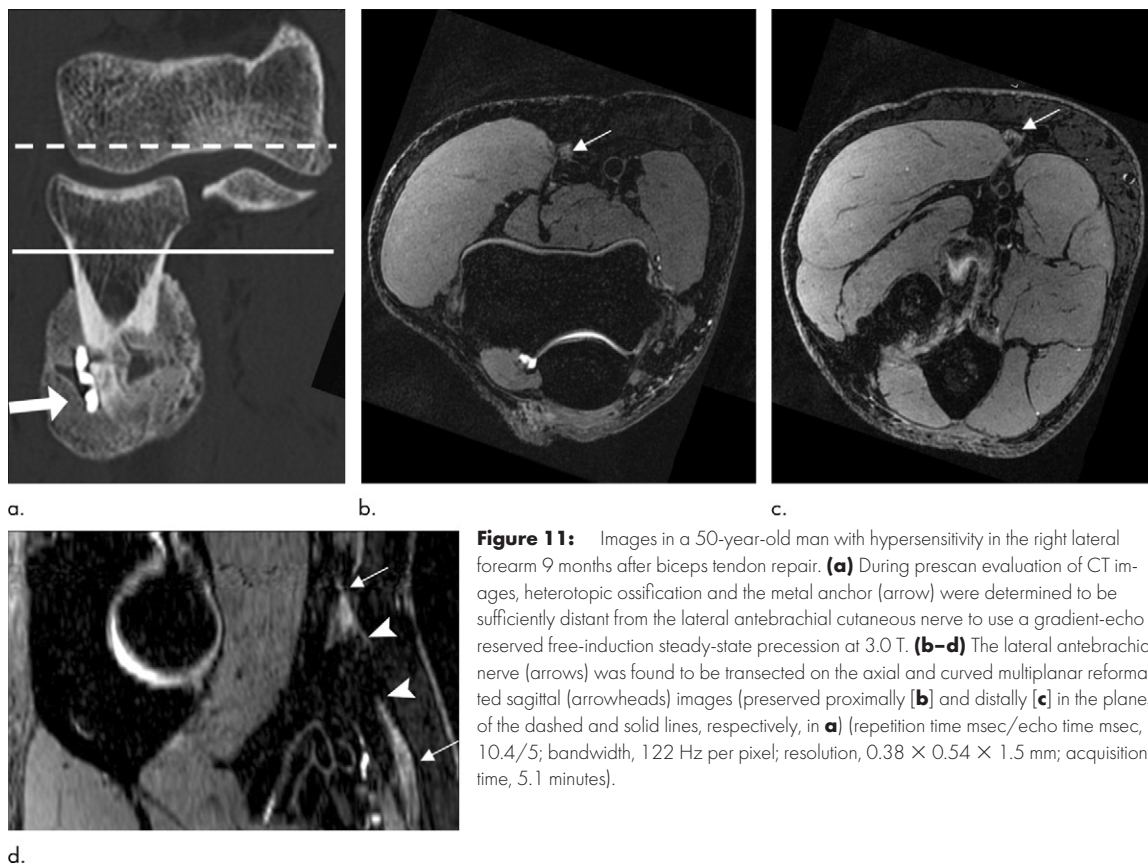


Figure 11: Images in a 50-year-old man with hypersensitivity in the right lateral forearm 9 months after biceps tendon repair. **(a)** During prescan evaluation of CT images, heterotopic ossification and the metal anchor (arrow) were determined to be sufficiently distant from the lateral antebrachial cutaneous nerve to use a gradient-echo reserved free-induction steady-state precession at 3.0 T. **(b–d)** The lateral antebrachial nerve (arrows) was found to be transected on the axial and curved multiplanar reformatted sagittal (arrowheads) images (preserved proximally **[b]** and distally **[c]** in the planes of the dashed and solid lines, respectively, in **a**) (repetition time msec/echo time msec, 10.4/5; bandwidth, 122 Hz per pixel; resolution, $0.38 \times 0.54 \times 1.5$ mm; acquisition time, 5.1 minutes).

Avoidance of gradient-echo sequences near metal.—Generally, gradient-recalled-echo sequences are not used when the presence of metal is known, especially when the nerve of interest is directly adjacent to orthopedic hardware. This is because the gradient-recalled-echo readout is not rephased as compared with FSE and is hence more susceptible to metal-related artifacts. However, when metal is not near, PSIF can be used for vascular suppression, which is particularly useful for visualization of small nerves that course along the blood vessels (Fig 11). The determination of whether a PSIF image will be clinically useful relies again on the prescribing radiologist's careful evaluation of each case and his or her understanding of the spatial relationship between the indwelling hardware and the nerve in question.

Future Directions

Interest in quantitative methods for PNI has increased in recent years. Diffusion-tensor imaging of the peripheral nerves may provide information related to their structural integrity (90). Quantitative muscle mapping with fat fraction mapping (91), T2 mapping, and diffusion imaging (92,93) may enable characterization of the extent of denervation to complement nerve imaging. However, quantitative MRI methods typically are not performed with 3D MSI; diffusion images are frequently acquired with echo-planar imaging readout and suffer from strong image distortions related to B_0 susceptibility. Fat fraction methods rely on accurate phase unwrapping, which can be challenging in the presence of strong B_0 susceptibility. In all, quantitative methods performed with conventional readouts would result in strong

signal dropout and image distortions that confound quantitative results. The 3D MSI methods for quantitative methods, such as diffusion imaging (94) and T2 mapping (95), have also been proposed for joint arthroplasty evaluation and would be promising methods for PNI evaluation near metal.

Conclusion

In conclusion, MR neurography is a useful and effective imaging modality with which to assess peripheral nerves adjacent to orthopedic hardware when pulse sequences are appropriately optimized. The techniques suggested here are guidelines, however, as each case must be considered individually, given the potential complexity of the artifact arising from the hardware and its spatial relationship to the nerves being evaluated.

Acknowledgments: The authors thank Dr Chee Yeong Lim, Dr Vivek Kalia, and Dr John Carrino for their contributions to this article.

Disclosures of Conflicts of Interest: D.B.S. Activities related to the present article: disclosed no relevant relationships. Activities not related to the present article: institution has a research agreement with GE Healthcare. Other relationships: disclosed no relevant relationships. K.C.Z. disclosed no relevant relationships. E.T.T. Activities related to the present article: disclosed no relevant relationships. Activities not related to the present article: was an employee of General Electric until 2019; lab receives institutional research support from GE Healthcare. Other relationships: disclosed no relevant relationships.

References

1. Welch MB, Brummett CM, Welch TD, et al. Perioperative peripheral nerve injuries: a retrospective study of 380,680 cases during a 10-year period at a single institution. *Anesthesiology* 2009;111(3):490–497.
2. Zywił MG, Mont MA, McGrath MS, Ulrich SD, Bonutti PM, Bhav A. Peroneal nerve dysfunction after total knee arthroplasty: characterization and treatment. *J Arthroplasty* 2011;26(3):379–385.

3. Upadhyay A, York S, Macaulay W, McGrory B, Robbenolt J, Bal BS. Medical malpractice in hip and knee arthroplasty. *J Arthroplasty* 2007;22(6 Suppl 2):2–7.
4. Cheney FW, Domino KB, Caplan RA, Posner KL. Nerve injury associated with anesthesia: a closed claims analysis. *Anesthesiology* 1999;90(4):1062–1069.
5. Hewson DW, Bedforth NM, Hardman JG. Peripheral nerve injury arising in anaesthesia practice. *Anaesthesia* 2018;73(Suppl 1):51–60.
6. Verdecchia N, Johnson J, Baratz M, Orebaugh S. Neurologic complications in common wrist and hand surgical procedures. *Orthop Rev (Pavia)* 2018;10(1):7355.
7. Fleischman AN, Rothman RH, Parvizi J. Femoral Nerve Palsy Following Total Hip Arthroplasty: Incidence and Course of Recovery. *J Arthroplasty* 2018;33(4):1194–1199.
8. Shetty T, Nguyen JT, Sasaki M, et al. Risk factors for acute nerve injury after total knee arthroplasty. *Muscle Nerve* 2018;57(6):946–950.
9. Carofino BC, Brogan DM, Kircher MF, et al. Iatrogenic nerve injuries during shoulder surgery. *J Bone Joint Surg Am* 2013;95(18):1667–1674.
10. Kelly EW, Morrey BF, O'Driscoll SW. Complications of elbow arthroscopy. *J Bone Joint Surg Am* 2001;83(1):25–34.
11. Wakana S, Jiang H, Nagae-Poetscher LM, van Zijl PC, Mori S. Fiber tract-based atlas of human white matter anatomy. *Radiology* 2004;230(1):77–87.
12. Leliveld MS, Verhofstad MHJ. Injury to the infrapatellar branch of the saphenous nerve, a possible cause for anterior knee pain after tibial nailing? *Injury* 2012;43(6):779–783.
13. Samson D, Power DM. Iatrogenic Injuries of the Palmar Branch of the Median Nerve Following Volar Plate Fixation of the Distal Radius. *J Hand Surg Asian Pac Vol* 2017;22(3):343–349.
14. Brown GD, Swanson EA, Nercessian OA. Neurologic injuries after total hip arthroplasty. *Am J Orthop (Belle Mead NJ)* 2008;37(4):191–197.
15. Ward JP, Yang LJS, Urquhart AG. Surgical decompression improves symptoms of late peroneal nerve dysfunction after TKA. *Orthopedics* 2013;36(4):e515–e519.
16. LiBrizzi CL, Rojas J, Joseph J, et al. Incidence of clinically evident isolated axillary nerve injury in 869 primary anatomic and reverse total shoulder arthroplasties without routine identification of the axillary nerve. *JSES Open Access* 2019;3(1):48–53.
17. Schwab TR, Stillhard PF, Schibli S, Furrer M, Sommer C. Radial nerve palsy in humeral shaft fractures with internal fixation: analysis of management and outcome. *Eur J Trauma Emerg Surg* 2018;44(2):235–243.
18. Cram P, Lu X, Kates SL, Singh JA, Li Y, Wolf BR. Total knee arthroplasty volume, utilization, and outcomes among Medicare beneficiaries, 1991–2010. *JAMA* 2012;308(12):1227–1236.
19. Singh JA, Yu S, Chen L, Cleveland JD. Rates of Total Joint Replacement in the United States: Future Projections to 2020–2040 Using the National Inpatient Sample. *J Rheumatol* 2019;46(9):1134–1140.
20. Sloan M, Premkumar A, Sheth NP. Projected Volume of Primary Total Joint Arthroplasty in the U.S., 2014 to 2030. *J Bone Joint Surg Am* 2018;100(17):1455–1460.
21. Fisher S, Wadhwa V, Manthuruthil C, Cheng J, Chhabra A. Clinical impact of magnetic resonance neurography in patients with brachial plexus neuropathies. *Br J Radiol* 2016;89(1067):20160503.
22. Gasparotti R, Padua L, Briani C, Lauria G. New technologies for the assessment of neuropathies. *Nat Rev Neurol* 2017;13(4):203–216.
23. Chhabra A, Andreisek G, Soldatos T, et al. MR neurography: past, present, and future. *AJR Am J Roentgenol* 2011;197(3):583–591.
24. Koff MF, Burge AJ, Koch KM, Potter HG. Imaging near orthopedic hardware. *J Magn Reson Imaging* 2017;46(1):24–39.
25. Koff MF, Burge AJ, Potter HG. Clinical magnetic resonance imaging of arthroplasty at 1.5 T. *J Orthop Res* 2020;38(7):1455–1464.
26. Zochowski KC, Miranda MA, Cheung J, et al. MRI of hip arthroplasties: Comparison of isotropic multiacquisition variable-resonance image combination selective (MAVRIC SL) acquisitions with a conventional MAVRIC SL acquisition. *AJR Am J Roentgenol* 2019;213(6):W277–W286.
27. Koff MF, Shah P, Potter HG. Clinical implementation of MRI of joint arthroplasty. *AJR Am J Roentgenol* 2014;203(1):154–161.
28. Wolf M, Bäumer P, Pedro M, et al. Sciatic nerve injury related to hip replacement surgery: imaging detection by MR neurography despite susceptibility artifacts. *PLoS One* 2014;9(2):e89154.
29. Cheung ZB, Patel AV, DeBellis N, Unis DB, Benitez CL. Sciatic Nerve Entanglement Around a Femoral Prosthesis During Closed Reduction of a Dislocated Total Hip Prosthesis: The Role of Metal-Suppression MRI: A Case Report. *JBJS Case Connect* 2018;8(1):e3.
30. Ahlawat S, Stern SE, Belzberg AJ, Fritz J. High-resolution metal artifact reduction MR imaging of the lumbosacral plexus in patients with metallic implants. *Skeletal Radiol* 2017;46(7):897–908.
31. Menorca RMG, Fussell TS, Elfar JC. Nerve physiology: mechanisms of injury and recovery. *Hand Clin* 2013;29(3):317–330.
32. Seddon HJ. Three Types Of Nerve Injury. *Brain* 1943;66(4):237–288.
33. Lee SK, Wolfe SW. Peripheral nerve injury and repair. *J Am Acad Orthop Surg* 2000;8(4):243–252.
34. Grinsell D, Keating CP. Peripheral nerve reconstruction after injury: a review of clinical and experimental therapies. *BioMed Res Int* 2014;2014:698256.
35. Pulos N, Shin EH, Spinner RJ, Shin AY. Management of Iatrogenic Nerve Injuries. *J Am Acad Orthop Surg* 2019;27(18):e838–e848.
36. Spinner RJ, Kline DG. Surgery for peripheral nerve and brachial plexus injuries or other nerve lesions. *Muscle Nerve* 2000;23(5):680–695.
37. Isaacs J. Major peripheral nerve injuries. *Hand Clin* 2013;29(3):371–382.
38. Trehan SK, Model Z, Lee SK. Nerve Repair and Nerve Grafting. *Hand Clin* 2016;32(2):119–125.
39. Dahlin LB. Techniques of peripheral nerve repair. *Scand J Surg* 2008;97(4):310–316.
40. Liss AG, af Ekenstam FW, Wiberg M. Loss of neurons in the dorsal root ganglia after transection of a peripheral sensory nerve. An anatomical study in monkeys. *Scand J Plast Reconstr Surg Hand Surg* 1996;30(1):1–6.
41. Ma J, Novikov LN, Kellerth JO, Wiberg M. Early nerve repair after injury to the postganglionic plexus: an experimental study of sensory and motor neuronal survival in adult rats. *Scand J Plast Reconstr Surg Hand Surg* 2003;37(1):1–9.
42. Lundborg G, Rosén B. Hand function after nerve repair. *Acta Physiol (Oxf)* 2007;189(2):207–217.
43. Dumitru D, Zwarts M. Needle Electromyography. In: Dumitru D, Amato A, Swarts M, eds. *Electrodiagnostic Medicine Pitfalls*. 2nd ed. Philadelphia, Pa: Hanley & Belfus, 2005; 541–577.
44. Feinberg J. EMG: myths and facts. *HSS J* 2006;2(1):19–21.
45. Howard FM Jr. Electromyography and conduction studies in peripheral nerve injuries. *Surg Clin North Am* 1972;52(5):1343–1352.
46. Brown BA. Internal neurolysis in traumatic peripheral nerve lesions in continuity. *Surg Clin North Am* 1972;52(5):1167–1175.
47. Du R, Auguste KL, Chin CT, Engstrom JW, Weinstein PR. Magnetic resonance neurography for the evaluation of peripheral nerve, brachial plexus, and nerve root disorders. *J Neurosurg* 2010;112(2):362–371.
48. Chhabra A, Carrino J. Current MR neurography techniques and whole-body MR neurography. *Semin Musculoskelet Radiol* 2015;19(2):79–85.
49. Martín Noguerol T, Barousse R, Gómez Cabrera M, Socolovsky M, Bencardino JT, Luna A. Functional MR Neurography in Evaluation of Peripheral Nerve Trauma and Postsurgical Assessment. *RadioGraphics* 2019;39(2):427–446.
50. Sneag DB, Queler S. Technological Advancements in Magnetic Resonance Neurography. *Curr Neurol Neurosci Rep* 2019;19(10):75.
51. Rangavajla G, Mokarram N, Masoodzadehgan N, Pai SB, Bellamkonda RV. Noninvasive imaging of peripheral nerves. *Cells Tissues Organs* 2014;200(1):69–77.
52. Zaidman CM, Seelig MJ, Baker JC, Mackinnon SE, Pestronk A. Detection of peripheral nerve pathology: comparison of ultrasound and MRI. *Neurology* 2013;80(18):1634–1640.
53. Toia F, Gagliardo A, D'Arpa S, Gagliardo C, Gagliardo G, Cordova A. Preoperative evaluation of peripheral nerve injuries: What is the place for ultrasound? *J Neurosurg* 2016;125(3):603–614.
54. Chhabra A, Belzberg AJ, Rosson GD, et al. Impact of high resolution 3 tesla MR neurography (MRN) on diagnostic thinking and therapeutic patient management. *Eur Radiol* 2016;26(5):1235–1244.
55. Wessig C, Koltzenburg M, Reiners K, Solymosi L, Bendszus M. Muscle magnetic resonance imaging of denervation and reinnervation: correlation with electrophysiology and histology. *Exp Neurol* 2004;185(2):254–261.
56. Chhabra A. Magnetic resonance neurography-simple guide to performance and interpretation. *Semin Roentgenol* 2013;48(2):111–125.
57. Chhabra A, Ahlawat S, Belzberg A, Andreisek G. Peripheral nerve injury grading simplified on MR neurography: As referenced to Seddon and Sunderland classifications. *Indian J Radiol Imaging* 2014;24(3):217–224.
58. Ohana M, Moser T, Moussaoui A, et al. Current and future imaging of the peripheral nervous system. *Diagn Interv Imaging* 2014;95(1):17–26.
59. Tagliafico A, Succio G, Emanuele Neumaier C, et al. MR imaging of the brachial plexus: comparison between 1.5-T and 3-T MR imaging: preliminary experience. *Skeletal Radiol* 2011;40(6):717–724.
60. Soher BJ, Dale BM, Merkle EM. A review of MR physics: 3T versus 1.5T. *Magn Reson Imaging Clin N Am* 2007;15(3):277–290, v.

61. Chhabra A, Flammang A, Padua A Jr, Carrino JA, Andreisek G. Magnetic resonance neurography: technical considerations. *Neuroimaging Clin N Am* 2014;24(1):67–78.
62. Carpenter EL, Bencardino JT. Focus on advanced magnetic resonance techniques in clinical practice: magnetic resonance neurography. *Radiol Clin North Am* 2015;53(3):513–529.
63. Dixon WT. Simple proton spectroscopic imaging. *Radiology* 1984;153(1):189–194.
64. Del Grande F, Santini F, Herzka DA, et al. Fat-suppression techniques for 3-T MR imaging of the musculoskeletal system. *RadioGraphics* 2014;34(1):217–233.
65. Tagliafico A, Bignotti B, Tagliafico G, Martinoli C. Usefulness of IDEAL T2 imaging for homogeneous fat suppression and reducing susceptibility artefacts in brachial plexus MRI at 3.0 T. *Radiol Med (Torino)* 2016;121(1): 45–53.
66. Chung YC, Merkle EM, Lewin JS, Shonk JR, Duerk JL. Fast T(2)-weighted imaging by PSIF at 0.2 T for interventional MRI. *Magn Reson Med* 1999;42(2):335–344.
67. Gyngell ML. The application of steady-state free precession in rapid 2DFT NMR imaging: FAST and CE-FAST sequences. *Magn Reson Imaging* 1988;6(4):415–419.
68. Busse RF, Hariharan H, Vu A, Brittain JH. Fast spin echo sequences with very long echo trains: design of variable refocusing flip angle schedules and generation of clinical T2 contrast. *Magn Reson Med* 2006;55(5):1030–1037.
69. Yoon D, Biswal S, Rutt B, Lutz A, Hargreaves B. Feasibility of 7T MRI for imaging fascicular structures of peripheral nerves. *Muscle Nerve* 2018;57(3):494–498.
70. Wang L, Niu Y, Kong X, et al. The application of paramagnetic contrast-based T2 effect to 3D heavily T2W high-resolution MR imaging of the brachial plexus and its branches. *Eur J Radiol* 2016;85(3):578–584.
71. Chen WC, Tsai YH, Weng HH, et al. Value of enhancement technique in 3D-T2-STIR images of the brachial plexus. *J Comput Assist Tomogr* 2014;38(3):335–339.
72. Wang J, Yarnykh VL, Hatsukami T, Chu B, Balu N, Yuan C. Improved suppression of plaque-mimicking artifacts in black-blood carotid atherosclerosis imaging using a multislice motion-sensitized driven-equilibrium (MSDE) turbo spin-echo (TSE) sequence. *Magn Reson Med* 2007;58(5):973–981.
73. Perdikakis E, Tsifountoudis I, Kalaitzoglou I, Rountas C, Malliaropoulos N, Maffulli N. Soft tissue pseudotumours: a pictorial review with emphasis on MRI. *Muscles Ligaments Tendons J* 2017;7(2):353–375.
74. Hargreaves BA, Worters PW, Pauly KB, Pauly JM, Koch KM, Gold GE. Metal-induced artifacts in MRI. *AJR Am J Roentgenol* 2011;197(3):547–555.
75. Schenck JF. The role of magnetic susceptibility in magnetic resonance imaging: MRI magnetic compatibility of the first and second kinds. *Med Phys* 1996;23(6):815–850.
76. Koch KM, Lorbiecki JE, Hinks RS, King KF. A multispectral three-dimensional acquisition technique for imaging near metal implants. *Magn Reson Med* 2009;61(2):381–390.
77. Bartusek K, Dokoupil Z, Gescheidtova E. Magnetic field mapping around metal implants using an asymmetric spin-echo MRI sequence. *Meas Sci Technol* 2006;17(12):3293–3300.
78. Duyn JH, Schenck J. Contributions to magnetic susceptibility of brain tissue. *NMR Biomed* 2017;30(4):e3546.
79. Eustace S, Goldberg R, Williamson D, et al. MR imaging of soft tissues adjacent to orthopaedic hardware: techniques to minimize susceptibility artefact. *Clin Radiol* 1997;52(8):589–594.
80. Lee MJ, Kim S, Lee SA, et al. Overcoming artifacts from metallic orthopedic implants at high-field-strength MR imaging and multi-detector CT. *RadioGraphics* 2007;27(3):791–803.
81. Raphael B, Haims AH, Wu JS, Katz LD, White LM, Lynch K. MRI comparison of periprosthetic structures around zirconium knee prostheses and cobalt chrome prostheses. *AJR Am J Roentgenol* 2006;186(6):1771–1777.
82. Gupta A, Subhas N, Primak AN, Nittka M, Liu K. Metal artifact reduction: standard and advanced magnetic resonance and computed tomography techniques. *Radiol Clin North Am* 2015;53(3):531–547.
83. Talbot BS, Weinberg EP. MR Imaging with Metal-suppression Sequences for Evaluation of Total Joint Arthroplasty. *RadioGraphics* 2016;36(1):209–225.
84. Jungmann PM, Agten CA, Pfirmann CW, Sutter R. Advances in MRI around metal. *J Magn Reson Imaging* 2017;46(4):972–991.
85. Tsai LL, Grant AK, Mortelet KJ, Kung JW, Smith MP. A Practical Guide to MR Imaging Safety: What Radiologists Need to Know. *RadioGraphics* 2015;35(6):1722–1737.
86. Khodarahmi I, Rajan S, Sterling R, Koch K, Kirsch J, Fritz J. Heating of Hip Arthroplasty Implants During Metal Artifact Reduction MRI at 1.5- and 3.0-T Field Strengths. *Invest Radiol* 2020. 10.1097/RLI.0000000000000732. Published online October 16, 2020https://doi.org/10.1097/RLI.0000000000000732.
87. Kaushik SS, Marszalkowski C, Koch KM. External calibration of the spectral coverage for three-dimensional multispectral MRI. *Magn Reson Med* 2016;76(5):1494–1503.
88. Szumowski J, Coshov WR, Li F, Quinn SF. Phase unwrapping in the three-point Dixon method for fat suppression MR imaging. *Radiology* 1994;192(2):555–561.
89. Hardy PA, Hinks RS, Tkach JA. Separation of fat and water in fast spin-echo MR imaging with the three-point Dixon technique. *J Magn Reson Imaging* 1995;5(2):181–185.
90. Godel T, Pham M, Kele H, et al. Diffusion tensor imaging in anterior interosseous nerve syndrome - functional MR Neurography on a fascicular level. *Neuroimage Clin* 2019;21:101659.
91. Duijnisveld BJ, Henseler JF, Reijnierse M, Fiocco M, Kan HE, Nelissen RG. Quantitative Dixon MRI sequences to relate muscle atrophy and fatty degeneration with range of motion and muscle force in brachial plexus injury. *Magn Reson Imaging* 2017;36:98–104.
92. Ha DH, Choi S, Kang EJ, Park HT. Diffusion tensor imaging and T2 mapping in early denervated skeletal muscle in rats. *J Magn Reson Imaging* 2015;42(3):617–623.
93. Holl N, Echaniz-Laguna A, Bierry G, et al. Diffusion-weighted MRI of denervated muscle: a clinical and experimental study. *Skeletal Radiol* 2008;37(12):1111–1117.
94. Koch KM, Bhavé S, Gaddipati A, et al. Multispectral diffusion-weighted imaging near metal implants. *Magn Reson Med* 2018;79(2):987–993.
95. Bhavé S, Koff MF, Sivaram Kaushik S, Potter HG, Koch KM. 3D-multi-spectral T₂ mapping near metal implants. *Magn Reson Med* 2019;82(2):614–621.
96. Sneag DB, Mendapara P, Zhu JC, et al. Prospective respiratory triggering improves high-resolution brachial plexus MRI quality. *J Magn Reson Imaging* 2019;49(6):1723–1729.
97. Farahani K, Sinha U, Sinha S, Chiu LC, Lufkin RB. Effect of field strength on susceptibility artifacts in magnetic resonance imaging. *Comput Med Imaging Graph* 1990;14(6):409–413.
98. Koch KM, Brau AC, Chen W, et al. Imaging near metal with a MAVRIC-SEMAC hybrid. *Magn Reson Med* 2011;65(1):71–82.